Journal of
*Marine Science and Engineering*

MDPI

*Article*

# Seasonal and Interannual Variability in Sea Surface Temperature Fronts in the Levantine Basin, Mediterranean Sea

**Anıl Akpınar**

Institute of Marine Sciences, Middle East Technical University (METU), Erdemli 33731, Türkiye; anil@ims.metu.edu.tr

**Abstract:** Sea surface temperature (SST) fronts were analyzed in the Levantine Basin of the Mediterranean Sea over a 20-year period (2003–2022) using a high-resolution (~1 km) satellite dataset. Frontal gradients were strongest in regions of freshwater influence and around the Ierapetra eddies and Rhodes Gyre. Seasonally, maximum frontal activity was observed in fall and summer. Empirical orthogonal function (EOF) analysis revealed both monthly-to-seasonal variability and interannual variability in frontal gradients. Seasonal frontal variability is partially explained by atmospheric forcing; that is, wind stress curl (WSC) and net air–sea heat flux. The maximum frontal activity was observed in 2006, coinciding with the strongest WSC magnitude. The minimum frontal activity was observed in 2017, which saw the largest winter heat loss to the atmosphere. The highest frontal activity was typically observed in years with mild winters followed by strong Etesian winds. Over the study period (2003–2022), frontal gradients declined in the Levantine Basin. Our results suggest that years with a strong frontal boundary current (Asia Minor Current; AMC) coincide with reduced cross-shelf transport. Subsequent studies are recommended to concentrate on the variability in the frontal intensity of the AMC and associated cross-shelf transports, which are important for the oligotrophic Levantine Basin.

**Keywords:** sea surface temperature; ocean fronts; Mediterranean Sea; seasonal and interannual variability; Levantine Basin; cross-shelf transport

check for updates

**Citation:** Akpınar, A. Seasonal and Interannual Variability in Sea Surface Temperature Fronts in the Levantine Basin, Mediterranean Sea. *J. Mar. Sci. Eng.* **2024**, *12*, 1249. https://doi.org/10.3390/jmse12081249

Academic Editor: João Miguel Dias

Received: 15 May 2024
Revised: 20 July 2024
Accepted: 22 July 2024
Published: 24 July 2024

**Copyright:** © 2024 by the author. Licensee MDPI, Basel, Switzerland. This article is an open access article distributed under the terms and conditions of the Creative Commons Attribution (CC BY) license (https://creativecommons.org/licenses/by/4.0/).

## 1. Introduction

Fronts are narrow areas with high gradients of physical and biogeochemical properties [1,2] in the ocean. Different types of fronts are formed through various physical processes, including shelf-break fronts, water mass fronts, and plume/coastal buoyancy fronts [1]. Regardless of their physical origin, these fronts often have chemical and biological gradients; furthermore, they are often associated with increased vertical fluxes [3] and enhanced productivity [2]. Fronts are also areas with strong ocean–atmosphere coupling [4–6].

Fronts are often investigated using satellite observations due to their synoptic coverage, with sea surface temperature (SST) data being the most frequently used [2]. In this study, SST data with ~1 km resolution were used to analyze fronts in the Levantine Basin of the Mediterranean Sea. The Mediterranean Sea is subject to abrupt impacts of climate change, including marine heatwaves [7–11], intense warming [12,13], rising sea levels, temperature, salinity, and freshwater fluxes [14] and, consequently, increased variability in the general circulation and water masses [14–21]. As ubiquitous features, fronts have been subject to various studies in the Mediterranean Sea. Specifically, SST fronts have been investigated in the Mediterranean for their coupling with the atmosphere [22,23]. Recently, an SST front dataset [24] has been presented for the Mediterranean Sea using a gradient-based detection algorithm and Lagrangian coherent structures. Apart from these studies, most of the efforts to understand fronts and frontal ecosystems have been concentrated in the Western Mediterranean, where fronts [25] and cross-front transport [26] have been investigated, along with their links to tuna fisheries [27]. Similar tuna fisheries

are also present in the Levantine Basin [28], but their association with frontal variability is unknown due to the scarcity of studies on SST fronts in the Eastern Mediterranean. Specifically, the persistence of fronts was studied over the Eastern Mediterranean using a 5 km dataset as part of a global investigation [29], and a brief analysis of frontal variability and cross-shelf transport in the Levantine Basin was presented in [30]. These studies, using data with ~5 km resolution, documented persistent fronts in the northwest of the Levantine Basin, particularly around the Ierapetra eddies and Rhodes Gyre [29], as well as the basin-wide cyclonic conduit [30]. Fronts were also detected using data with ~1 km resolution, accompanied by Lagrangian analysis to document ecological provinces [24]. Although these studies provide an overall understanding of fronts in the region, they do not discuss the temporal and spatial variability in fronts in the Levantine Basin.

In this study, we investigated the temporal and spatial variability in SST fronts in the Levantine Basin using a 20-year (2003–2023) dataset with ~1 km resolution. The aim of this study was to investigate the temporal and spatial variability in fronts and to provide a basis for future studies linking SST fronts with ecosystem studies (e.g., primary productivity and tuna fisheries). This study provides the following:

- The temporal and spatial variability in fronts in the Levantine Basin at high (~1 km) resolution, for the first time.
- Relationships of major forcing (wind and heat flux) and frontal variability.
- The frontal variability in boundary currents and associated cross-shelf transport.

Our data and methods are presented in Section 2. The results are presented in Section 3. Seasonal climatology of SST and SST gradients are provided in Section 3.1, and frontal variabilities in seasonal and interannual timescales are presented in Sections 3.2 and 3.3, respectively. Case studies documenting the frontal variability in the Asia Minor Current and associated cross-shelf transports are presented in Section 3.4. Section 4 presents the Discussion and, finally, our conclusions and future prospects are given in Section 5.

## 2. Materials and Methods

This study uses the Multi-scale Ultra-high Resolution (MUR) sea surface temperature (SST) analysis [31] data (hereafter, MURSST), obtained from the Physical Oceanography Distributed Active Archive Center. The dataset used in this study consists of 30 years (2003–2022) of daily global SST images with 0.01° spatial resolution. The study area is limited by the 24 °E meridian in the west and 37° latitude in the north, as shown in Figure 1.

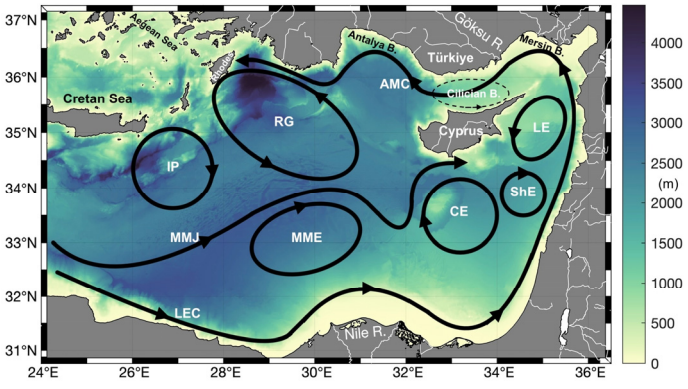



**Figure 1.** Bathymetric map of the Levantine Basin. Major rivers are shown in white. Major circulation features are overlaid using previous studies [14,17,32,33]. MMJ: Mid-Mediterranean Jet, AMC: Asia Minor Current, LEC: Libyo-Egyptian Current, RG: Rhodes Gyre, IP: Ierapetra eddies, ShE: Shikmona eddies, LE: Latakia eddies, CE: Cyprus eddies, MME: Mersa-Matruh eddies. Mersin B. and Antalya B. denote Mersin Bay and Antalya Bay, respectively. A quasi-persistent cyclone in the Cilician Basin [17] is shown with a dashed oval.

Thermal gradient magnitudes and the Canny edge detection algorithm [34] were used to identify frontal regions and their seasonal variability in the Levantine Basin. SST gradient magnitude (∇SST) was computed as follows:

$$\nabla \mathrm{SST} = \sqrt{(\nabla_x SST)^2 + (\nabla_y SST)^2}$$

where $\nabla_x$SST and $\nabla_y$SST denote the directional gradients computed over a three-by-three grid cell.

In order to define fronts, the Canny edge detection algorithm [34], a widely used method in oceanic front detection [2,5,35], was applied to the daily SST images. As a first step in this algorithm, the SST image is smoothed with a Gaussian filter prior to gradient calculation. In the second step, the gradient of the image is calculated using the derivative of a Gaussian filter with a 16 × 16 window size and a sigma value of $\sqrt{2}$. The third step is non-maximum suppression, which briefly results in thinner edges. The final step of the Canny algorithm is hysteresis thresholding, where upper and lower thresholds are used to find strong and weak edges. If the gradient magnitude of a pixel is larger than the upper threshold, it is defined as a front. The algorithm then tracks the frontal pixels until the gradient magnitude is less than the lower threshold. The thresholds employed in this study were determined by investigating the distribution of gradient magnitudes. An example sequence of the frontal detection procedure for a daily SST image is provided in the Supplementary Materials (Figure S1).

The 70th and 90th percentiles of the gradient magnitudes are shown in Figure 2a,b, respectively, while the probability density function (PDF) is shown in Figure 2c. The basin means of the 70th percentile and 90th percentile gradient magnitudes were 0.032 °C/km and 0.056 °C/km, respectively. The gradient magnitudes often exceeded 0.1 °C/km in areas of strong frontal activity, particularly around the Ierapetra eddies and Rhodes Gyre, as well as in regions of freshwater influence (ROFI) such as the Nile River discharge area and Mersin Bay, where major rivers discharge. Therefore, in this analysis, 0.1 °C/km was used as the higher threshold (and 0.05 °C/km as the lower threshold) for the Canny algorithm, distinguishing most of the gradient magnitudes in the upper range of PDF distribution (Figure 2c).

Frontal probability (FP) was defined as follows:

$$\mathrm{FP} = \left(\frac{\mathrm{N}}{\mathrm{T}}\right) \times 100\%$$

where N is the number of times a pixel is identified as a frontal pixel and T is the total number of satellite images (e.g., a season) over which the FP is calculated.

Absolute dynamic topography (ADT) and geostrophic velocity data were obtained from the Copernicus Marine Service (CMEMS) gridded sea surface height data for European seas, which consist of the optimally interpolated along-track data from available altimetry missions. Kinetic energy per unit mass (KE) was calculated from the geostrophic velocity data as follows:

$$KE = \frac{1}{2}\left(U_g^2 \pm V_g^2\right)$$

where $U_g$ and $V_g$ are the zonal and meridional geostrophic velocities, respectively.

The satellite chlorophyll-a dataset was obtained from CMEMS. This is a gap-free, multi-platform chlorophyll-a dataset with ~1 km resolution [36–38].

Wind (10 m eastward and northward components) and heat flux data were obtained from ERA5 reanalysis [39,40]. Wind stress curl (hereafter, WSC) was calculated using zonal and meridional wind stress. Air-to-sea net heat flux (hereafter, HF) was calculated as the sum of latent, sensible, short-wave, and long-wave components. Negative values of HF indicate heat loss to the atmosphere.

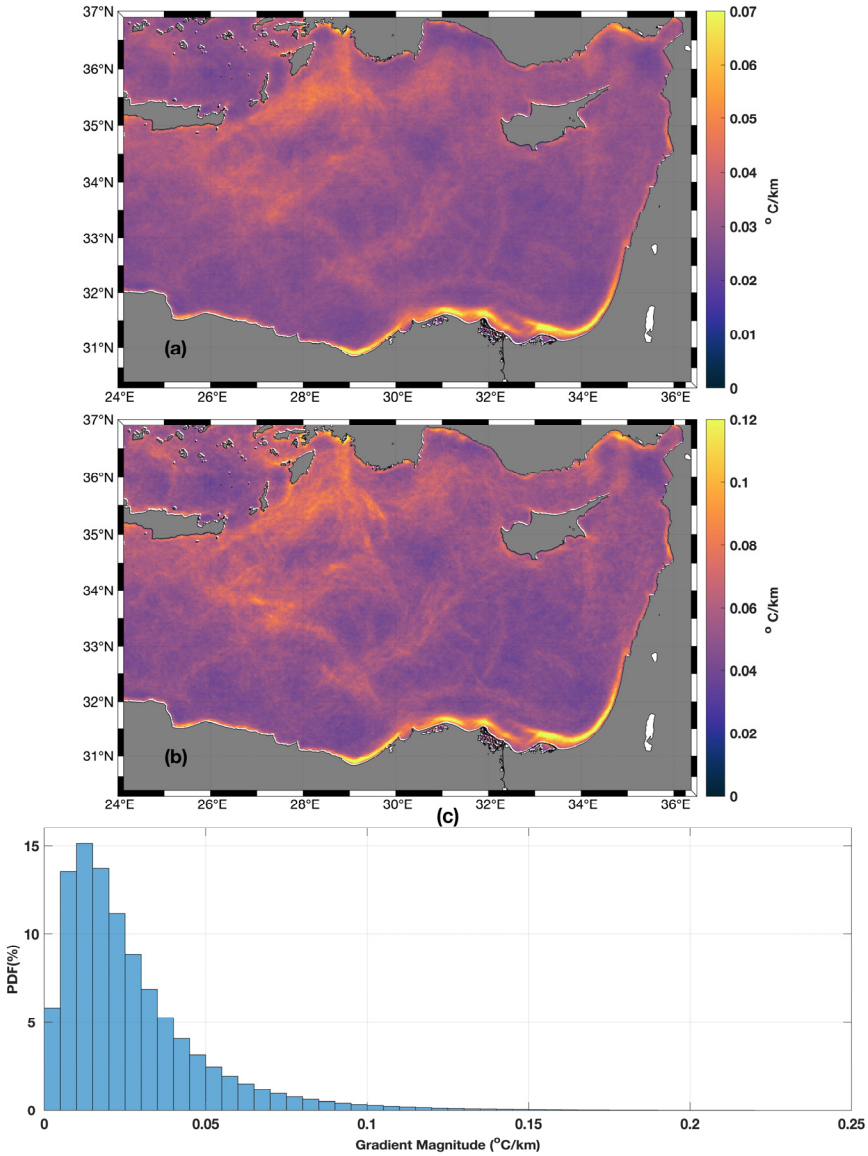



**Figure 2.** (**a**) The 70th percentile of the SST gradients. (**b**) The 90th percentile of the SST gradients. (**c**) Probability density function of the SST gradients over the study period for the whole Levantine Basin.

In this study, our primary interest was the variability at monthly-to-interannual scales. Hence, EOF analysis was performed on datasets of monthly mean SST gradients, WSC, and HF to determine their temporal and spatial variability. This analysis was repeated for the SST gradients, after removing the annual cycle, to investigate their interannual variability. Throughout the text, "EOF-1, PC-1", and so on refer to the seasonal EOF analysis, while "EOF1-INT, PC1-INT", and so on refer to the interannual EOF components of SST gradients (i.e., EOF analysis conducted after removing the seasonal cycles). The EOF modes of WSC and HF are denoted clearly as "EOF1-WSC", "PC1-HF", and so on.

Climatology of the SST, SST gradients, and KE provided in the Supplementary Materials was constructed for each month. Monthly climatology refers to the mean value of a variable for each month, where the mean is computed over the 20-year study period (2003–2022). For example,

$$January\ Climatology = Mean\ (January_{2003}, January_{2004}, \ldots.., January_{2022})$$

Bathymetry of the Levantine Basin was obtained from [41]. Figures were generated using functions from "m_map" [42], "cmocean" [43], and "Climate Data Toolbox" [44].

## 3. Results

### 3.1. Seasonal Climatology of SST and SST Gradients

The seasonal climatology of sea surface temperature (SST) (Figure 3) shows a northwest–southeast transition in almost every season. Winter SST (Figure 3) shows waters with temperatures between 16.5 °C and 17.5 °C in the Cretan Sea and the Aegean Sea further north, but also around the Rhodes Gyre, and waters between 17.5 °C and 18 °C at the coast. SSTs of 18.5 °C can be observed on a southwest–northeast path, reaching the Latakia Basin in the northeast and further extending along the coast of Türkiye, characteristic of well-known [33,45] circulation features (i.e., the Mid-Mediterranean Jet and Asia Minor Current). Warmer SSTs around 26° E and 34° N signal the imprint of Ierapetra eddies. Southern and southeastern Levantine waters have the highest temperatures, with a mean exceeding 19 °C. In spring, SST shows an east–west transition, with colder waters around the Rhodes Gyre. Although a similar spatial pattern to winter exists west of 31° E, it does not exist to its east. Instead, east of 31° N, SST has low variability, with typical values of ~19.5 °C. In summer, the SST signal around the Rhodes Gyre moves further west, and the seasonal mean SST exceeds 28 °C east of 30° E. In fall, a stronger northwest–southeast SST transition is visible, with temperatures exceeding 26 °C along the eastern coastline. Here, the seasonal climatology of SST is presented as a basis for SST gradients. The temporal and spatial distribution of SST has been presented in detail in previous studies [13,46,47] and the references therein.

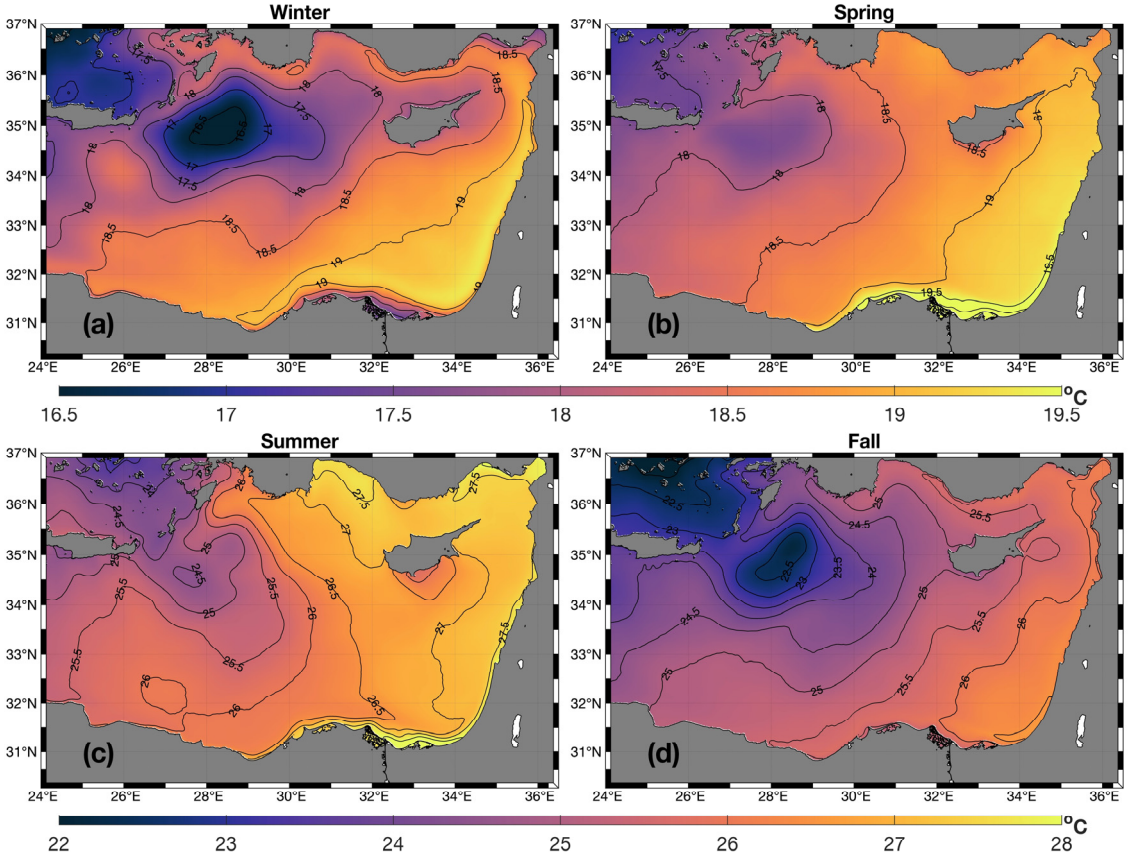



**Figure 3.** Seasonal climatology of SST in the Levantine Basin for (**a**) winter, (**b**) spring, (**c**) summer, and (**d**) fall. Winter and spring have the same color bar, and summer and fall share the same color bar.

The seasonal climatology of the SST gradients computed over 20 years (2003–2022), along with their standard deviations, is shown in Figure 4. The strongest SST gradient

magnitudes are observed at the coast, where major rivers discharge (e.g., Nile River, Mersin Bay), regardless of the season. Other than these regions, the strongest SST gradients are observed around the Rhodes Gyre due to its colder waters (Figure 3).

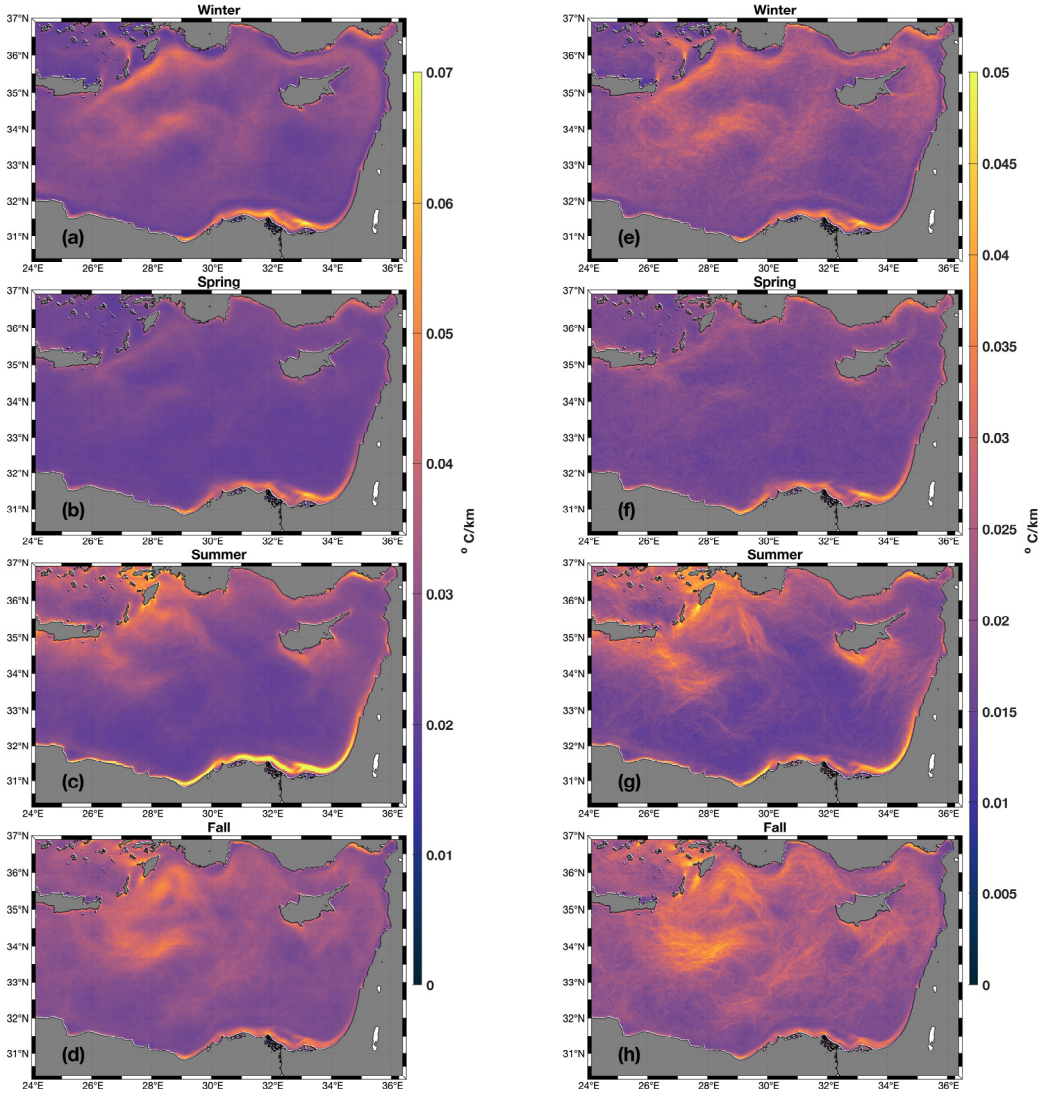



**Figure 4.** (**a**–**d**) Seasonal climatology of SST gradients, and (**e**–**h**) corresponding standard deviations.

In winter, the strongest SST gradients are observed (Figure 4a) in the north, consistent with the SST pattern (Figure 3), corresponding to major circulation features [32,33]. In spring (Figure 4b), the SST gradient magnitudes are lower than 0.04 °C/km basin-wide, except in ROFI. The lowest basin-wide SST gradients in spring correspond to decreased wind forcing and increased warming. In summer (Figure 4c), the SST gradients intensify, particularly at the coast, exceeding 0.04 °C/km, except for the Mersin Bay and Nile River discharge areas, where they exceed 0.07 °C/km. Coastal areas around Rhodes have slightly higher SST gradient magnitudes compared to other parts of the coastline, exceeding 0.05 °C/km. The SST gradients in fall (Figure 4d) are around 0.05 °C/km at the coastline, weaker than their summer values. The SST gradients in fall are stronger in the northern Levantine waters, locally exceeding 0.04 °C/km and resembling the pattern observed in winter. Stronger SST gradients are clearly visible around the Rhodes Gyre (Figure 4d).

### *3.2. Frontal Variability at Seasonal Timescales*

The Canny edge detection algorithm was used to define fronts and calculate the seasonal frontal probabilities (FPs), which are shown in Figure 5. In all seasons, the

maximum frontal probability was found around ROFI, consistent with the occurrence of the largest SST gradient magnitudes (Figure 4). In winter, the FP (Figure 5a) around major river discharge areas (i.e., the Nile River and Mersin Bay) ranges from 8% to 11%, and from around 5% to 8% in the rest of the northern Levantine waters, with the exception of the Rhodes Gyre, an FP of 7–10%. In spring, the FP distribution (Figure 5b) is rather fuzzy compared to winter but shows similar patterns. In spring, apart from ROFI, the largest FPs are found in the northern Levantine waters, similar to winter, but the FP percentages are different. In spring, the FP is 6–8% around Ierapetra and Rhodes Gyre, 5–7% in the rest of the northern Levantine waters, and typically around 5% in the southern Levantine waters. In summer (Figure 5c), the FP is high all along the coast, often exceeding 10%. Fronts occur 8–11% of the time southwest of Crete and Rhodes, and around 7–9% of the time southwest of Cyprus. In fall, the FP is 9–11% and 7–9% in the areas where the Rhodes Gyre and Ierapetra eddies typically occur, respectively. With these exceptions, the FP distribution is typically 8% around the basin, although higher values are typically observed in the northern Levantine waters (north of 33° N). The spatial distribution of FP in fall (Figure 5d) resembles that in winter (Figure 5a), with higher values corresponding to major circulation features, but it is noisier.

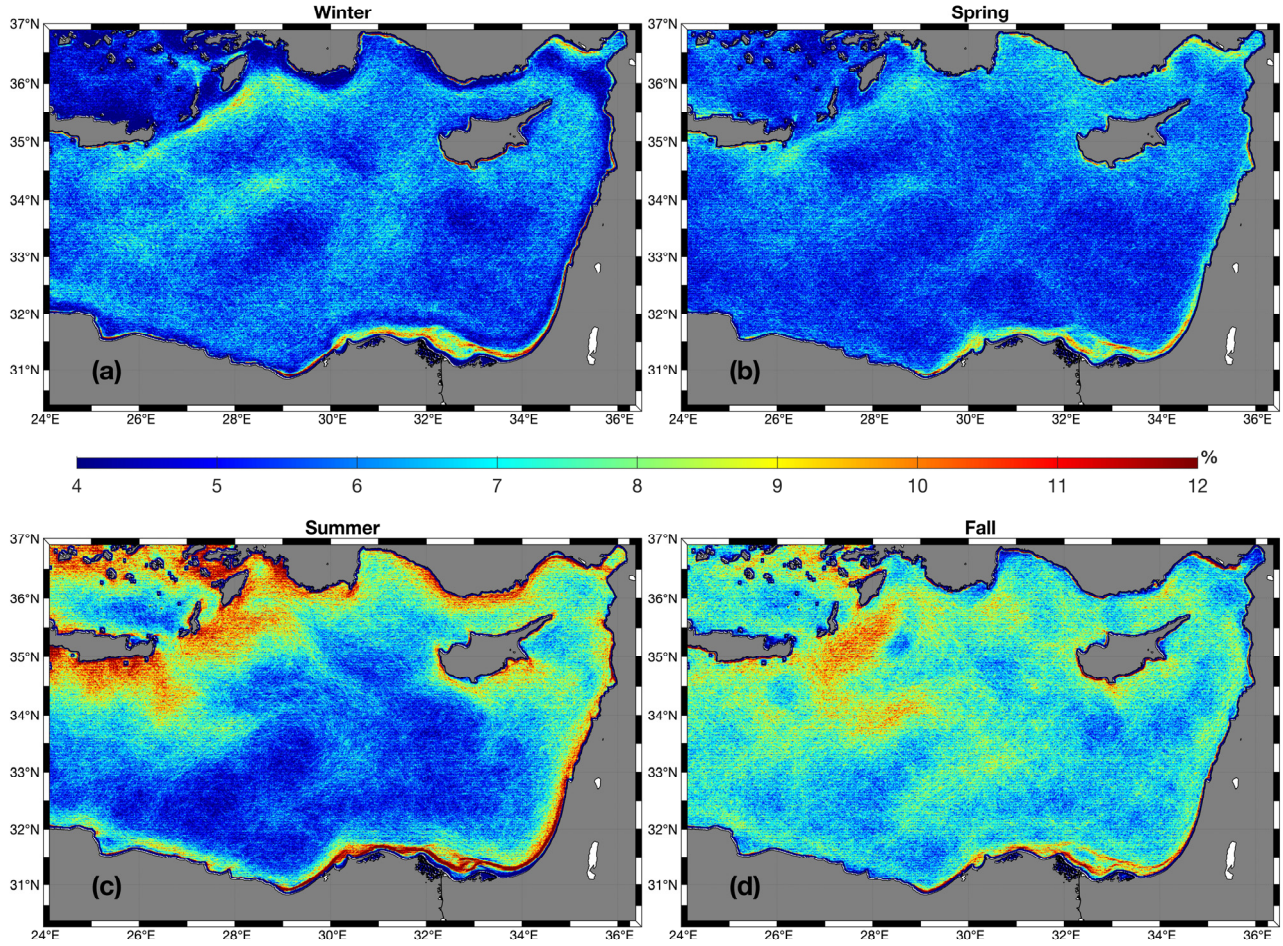



**Figure 5.** Frontal probabilities calculated for each season: (**a**) winter, (**b**) spring, (**c**) summer, and (**d**) fall.

Following the seasonal distribution of SST gradient magnitudes and frontal probability, an EOF analysis of the SST gradient magnitudes was carried out to determine the main modes of variability. The first two EOF spatial modes (EOF) and their principal component time series (PC) are shown in Figure 6, which represent 48.7% and 25.4% of the variance, respectively. The first EOF mode (Figure 6a) represents frontal magnitudes in the northern

Levantine waters (north of 33° N). The mean annual cycle of the first PC (Figure 6c) shows a clear weakening of the gradient magnitudes in April and a strengthening after June, with maximum values in November. PC1 also displays interannual variability, with its maximum value in 2006 (November) and minimum value in 2017 (April). The second EOF mode (Figure 6b) displays a clear separation of the coastal and offshore waters, with positive (negative) PC values corresponding to increased (decreased) coastal gradient magnitudes. Negative PC values also correspond to an increase in offshore gradient magnitudes, particularly south of the Rhodes Gyre. Its annual mean cycle (Figure 6c) shows increased magnitudes in summer, with a peak in July, and minimum values between October and December. PC2 had its maximum positive values in July 2020 and its negative values in November 2006.

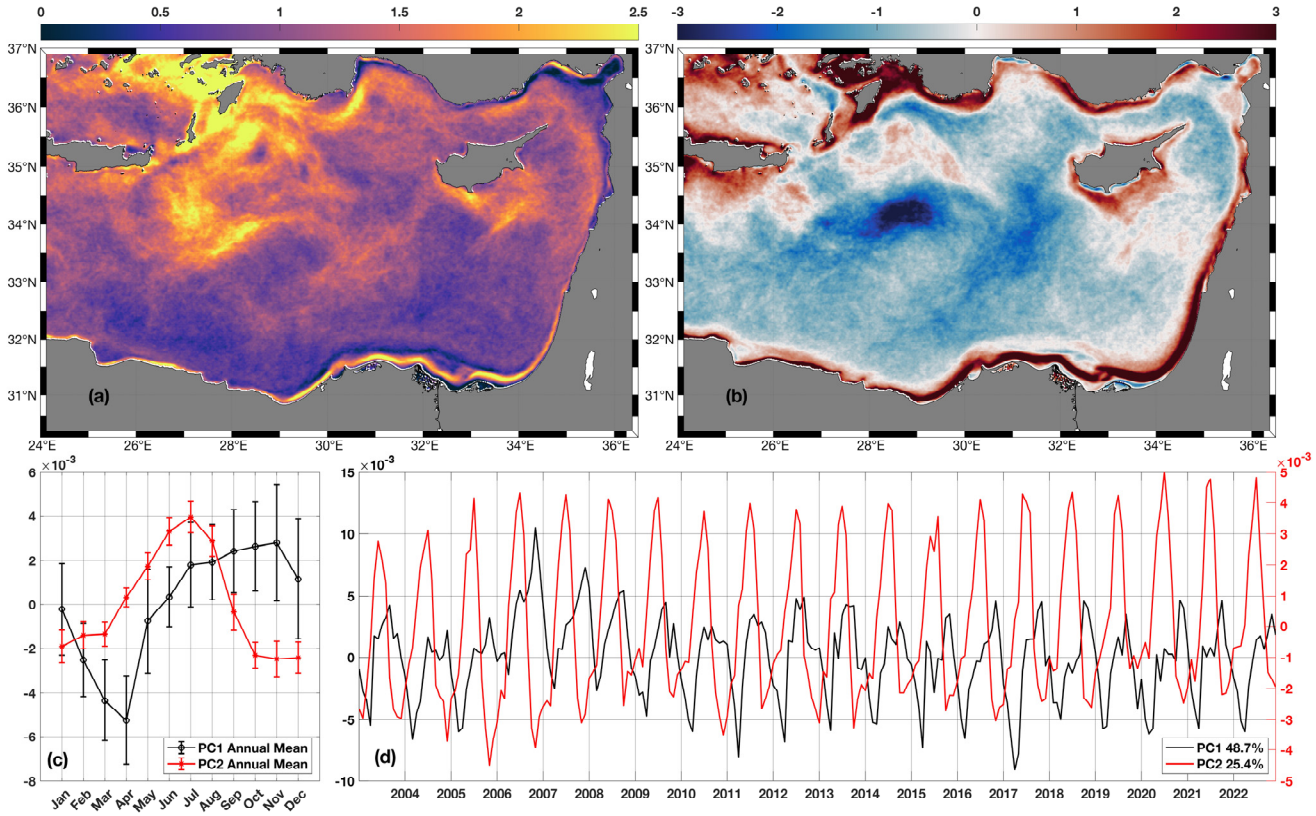



**Figure 6.** EOF maps for (**a**) first mode and (**b**) second mode. (**c**) Annual means of PC1 and PC2 time series. (**d**) Temporal evolution of the principal components (PC1 and PC2). Explained variances for the first and second EOF modes are 48.7% and 25.4%, respectively.

Wind stress curl (WSC) and air–sea heat flux (HF) were used as two major forcings of the general circulation. The first EOF modes of wind stress curl (EOF1-WSC) and net air–sea heat flux (EOF1-HF), along with the time series of the principal components (PC1-WSC and PC1-HF, respectively), are shown in Figure 7, explaining 70% and 98.7% of the variance, respectively, both representing their seasonal cycles. Annually (Figure 7c), PC1-WSC and PC1-HF have their maximum magnitudes in July and June, respectively.

EOF1-WSC displays (Figure 7a) opposite signs around Rhodes Gyre and Crete, as well as dipoles to the west and north of Cyprus. Positive values of PC1-WSC correspond to increased negative (anticyclonic) curl, which generates the Ierapetra eddies [48–51]. EOF1-HF displays the largest values in the north (Antalya and Cilician Basins) and around Ierapetra (Figure 7b). Positive values of PC1-HF correspond to extensive summer heating, while negative values correspond to winter cooling.

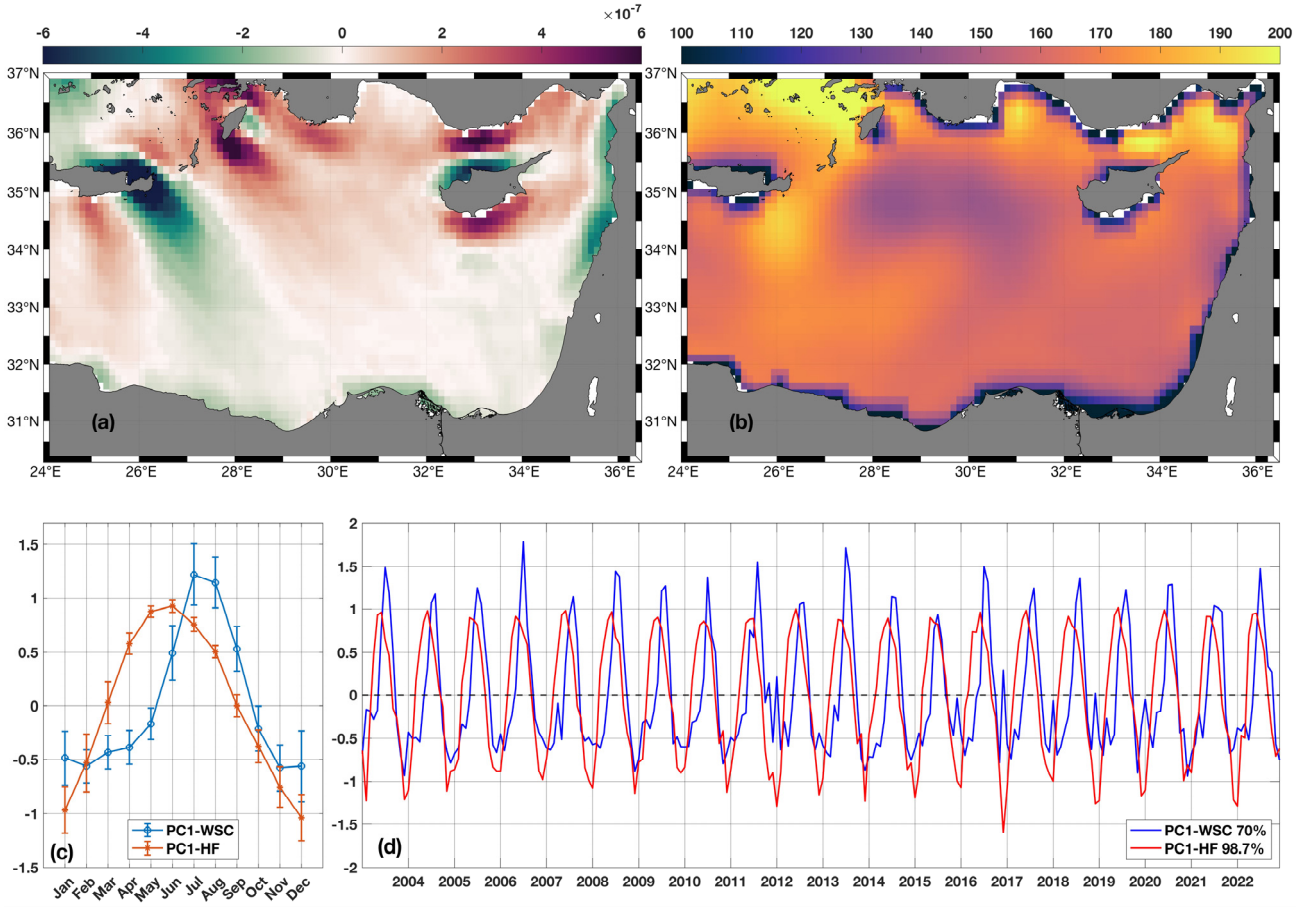



**Figure 7.** First EOF modes for (**a**) wind stress curl and (**b**) heat flux; (**c**) annual means of their time series. (**d**) Temporal evolution of the principal components (WSC-1 and HF-1). Explained variances for the first EOF modes of WSC and HF are 70% and 98.7%, respectively.

The seasonal variability in SST gradients (PC1, Figure 6d) can be partially explained by the variability in WSC or HF. For instance, the maximum PC1 value (Figure 6d) in fall 2006 corresponds to a period of maximum WSC (Figure 7d), which particularly intensifies the general circulation—specifically, the anticyclonic (cyclonic) circulation of Ierapetra eddies (Rhodes Gyre). Coherently, 2006 (along with 2010) shows the least winter heat loss to the atmosphere. The maximum winter cooling of the whole period was in winter 2017 (Figure 7d), corresponding to the minimum PC1 value (Figure 6d) in spring 2017. In addition to these coherent signals, seasonal variability in SST gradients has statistically significant correlations with wind and heat flux. PC1 (Figure 6d) and PC1-WSC (Figure 7d) have a correlation of r = 0.72 with 4 months of lag. PC2 (Figure 6d) and PC1-HF have a correlation of r = 0.84.

November 2006 (along with November 2005) also has a peak PC2 value (negative) (Figure 6d), which represents decreased SST gradient magnitudes at the coast and increased SST gradient magnitudes offshore, most significantly south of Rhodes Gyre (around 29° E and 34° N). PC2 displays increasing positive values starting from 2015 (Figure 6d), representing the intensification of coastal SST gradients in summer. Coastal SST gradients' variability (Figure 6b) spatially corresponds to areas occupied by boundary currents.

### *3.3. Frontal Variability at Interannual Timescales*

The monthly-to-seasonal variability presented above displays the weakest and most intense frontal activity in 2017 and 2006, respectively. Here, the annual means of basin-averaged SST gradients and FP are presented, both of which were also lowest in 2017 and highest in 2006 (Figure 8), as a result of the extensive winter cooling (in 2017) and intense

wind forcing (in 2006). The minimal winter heat loss accompanied by the strongest WSC pattern in 2006 corresponds to the highest annual basin-averaged SST gradients and FP (Figure 8). This confirms the intensification/weakening of the fronts throughout the basin, concurrent with the intensification/weakening of the heat flux and wind forcing.

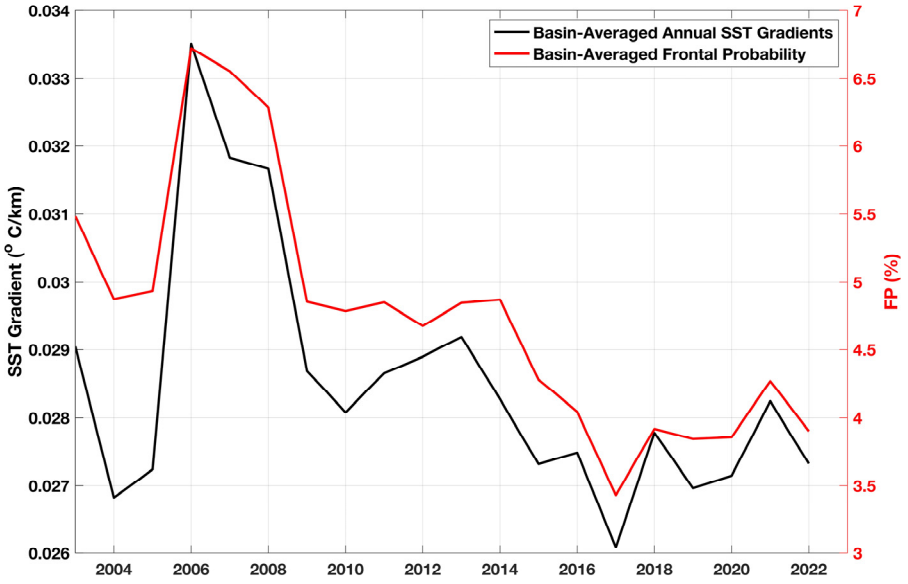



**Figure 8.** Basin-averaged annual means of SST gradients (left *y*-axis) and frontal probability (right *y*-axis).

The basin-averaged annual means of SST gradients and FP (Figure 8) provide a general understanding, but they do not present spatial variability. Spatial variability in frontal activity is shown with EOF analysis on SST gradients (Figure 6), which mainly represents monthly-to-seasonal variability. Therefore, to provide an understanding of the interannual variability in frontal activity, the seasonal cycle was removed from the SST gradient dataset, and EOF analysis was repeated on the de-seasoned dataset. The first and second interannual EOF modes (EOF-INT) explain 52.1% and 17.6% of the total variance, respectively. EOF1-INT (Figure 9a) shows a well-defined structure, indicating maximum values at the coasts as well as in the northwestern part of the basin, particularly around the Rhodes Gyre and Ierapetra areas, as well as southeast of Cyprus (~34° N) and west of Antalya Bay (~36–36.5° N and 30.5° E); it also displays variability in southern Levantine waters (32–33° N band). Similar to the results on a seasonal scale, this mode captures the variability corresponding to areas of well-known circulation features. Positive values of its time series (PC1-INT, Figure 9c) imply an intensification of gradient magnitudes for these areas. PC1-INT has a positive maximum between 2006 and 2009, a positive–negative phase between 2009 and 2014, and switches to a negative phase after 2014, implying a reduction in SST gradient magnitudes.

EOF2-INT (Figure 9b) shows positive values at the coast and mostly in the northern Levantine waters, and negative values elsewhere, mostly in the south; its time series (PC2-INT) shows (Figure 9c) negative maxima for 2003–2006, followed by positive/negative oscillations with weaker amplitudes until 2017, and stronger positive values during 2018–2022. Overall, EOF2-INT (Figure 9b) represents an increase in SST gradient magnitude in coastal zones and mostly northern Levantine waters, whereas EOF1-INT represents a basin-wide reduction in SST gradient magnitudes over the time series.

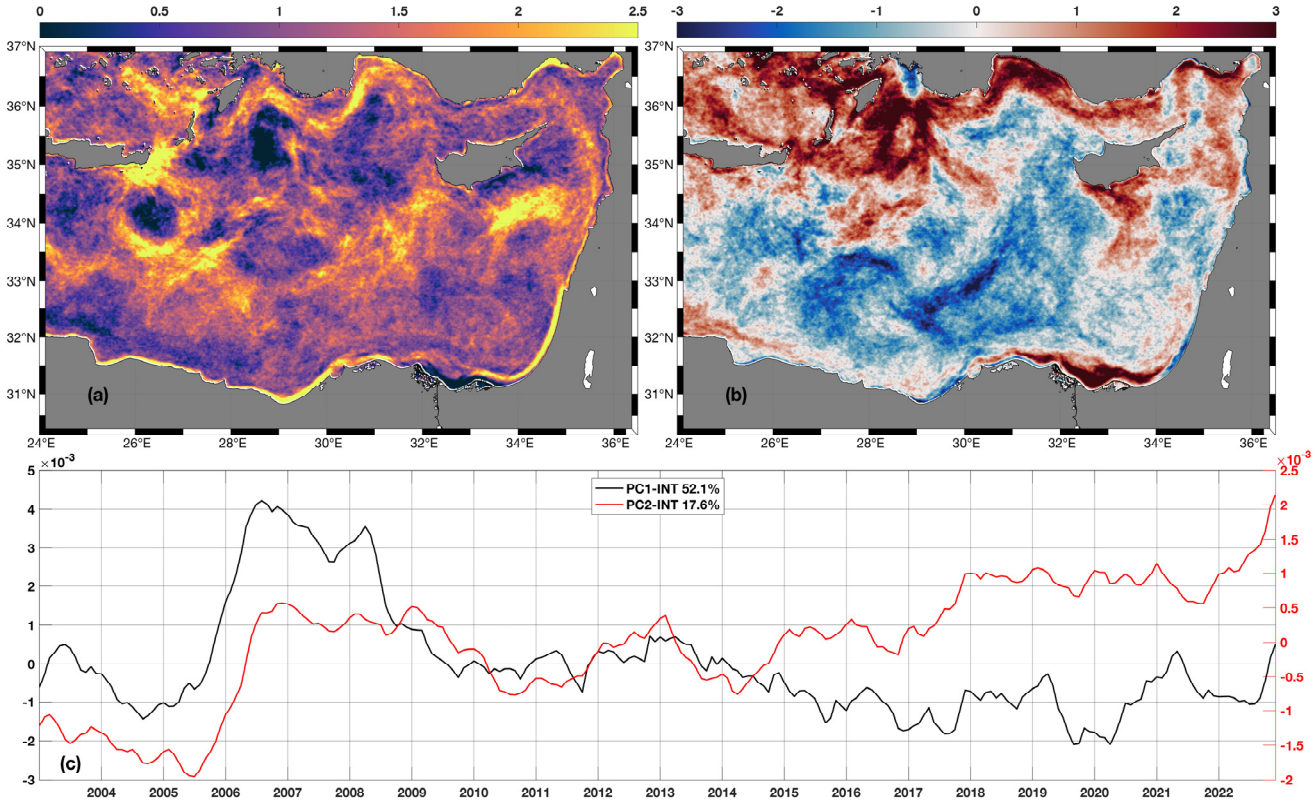



**Figure 9.** Interannual EOF modes for the (**a**) first mode (EOF1-INT), (**b**) second mode (EOF2-INT), and (**c**) their temporal evolution (PC1-INT and PC2-INT). Explained variances for the first and second interannual EOF modes are 52.1% and 17.6%, respectively.

### *3.4. Frontal Variability in the Asia Minor Current and Associated Cross-Shelf Transport*

In this section, a major boundary current in the Levantine Basin—the Asia Minor Current (AMC)—is investigated, which is known for its strong frontal gradient and cyclonic/anticyclonic bimodal circulation in summer [45]. A section of the AMC in the northeastern Levantine waters (i.e., the Cilician Basin) was investigated for its summertime frontal variability.

Typically, the AMC is strong in winter (December–February), as documented by high kinetic energy (Figure S2), and has a pronounced north–south SST gradient (Figure S3). With the onset of stratification in spring, the AMC weakens (lower kinetic energy) and the north–south SST gradient disappears. Instabilities in the AMC lead to filaments and eddy generation, which are conduits for cross-shelf transport. A cyclone ([12,16,17]) can be observed between Türkiye and Cyprus. The imprint of this cyclone is even observed in the monthly SST climatology (Figure S4), with colder SST due to enhanced upwelling. In summer, anticyclonic eddies are also observed [45] in the Cilician Basin. Kinetic energy increases due to strong summer winds (i.e., Etesians), but the strong frontal gradients of the AMC are not present. Instead, in summer, strong frontal gradients are observed at the coast. The summer maximum of kinetic energy is observed in August. In fall, kinetic energy is reduced as the Etesians weaken and is accompanied by gradual heat loss to the atmosphere. Eventually, the AMC intensifies again in December, represented by higher frontal gradients and high kinetic energy.

Here, the summer conditions of 2018 and 2020 are presented as two different cases in the northeastern Levantine waters. Summer 2020 was selected because it had the strongest gradient magnitudes, as confirmed by the positive maxima (PC2; Figure 6d), and 2018 was chosen to represent a recent year with weaker gradient values in order to show the difference between years with strong and weak frontal gradients.

The monthly averaged summer (i.e., June–August) absolute dynamic topography and superimposed geostrophic currents are shown in Figure 10 for 2018 and 2020. In 2020, eddies were present in June, but the circulation intensified in July/August, resulting in the disappearance of eddies and the appearance of a pronounced boundary current. Meanwhile, in 2018, the Asia Minor Current was weaker, with meanders and eddies present. A cyclone/anticyclone dipole existed throughout the summer of 2018 between 32° E and 34° E (and between Cyprus and Türkiye). Cross-shelf transport occurred throughout the summer via these eddies. Figure 11 shows the cross-shelf transport of waters with chlorophyll-a (Chl-a) values exceeding ~0.05 mg/m$^3$, which is a significant amount for the oligotrophic Levantine waters. In June, eddy dipoles carry waters offshore (Figure 11a), whereas in July (Figure 11b), high-Chl-a waters are observed on the periphery of the cyclonic eddy, and in August (Figure 11c), a high-Chl-a patch is on the periphery of the coastal anticyclone, showing that all of the observed features contribute to the cross-shelf transport of chlorophyll-rich coastal waters.

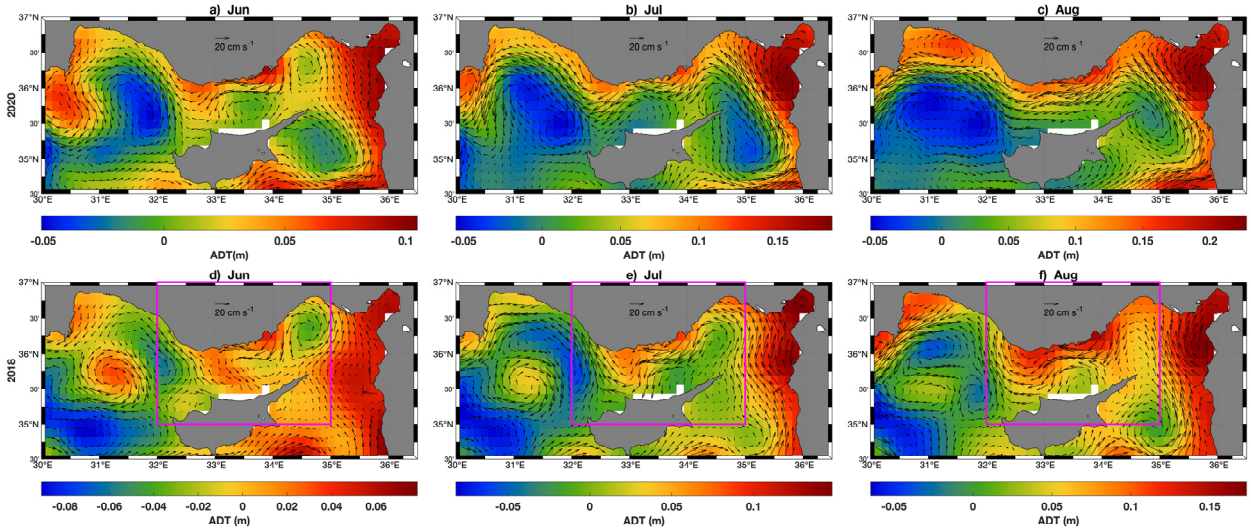



**Figure 10.** Absolute dynamic topography (meters) with superimposed geostrophic velocities for the summer (June–August) of (**a**–**c**) 2020 and (**d**–**f**) 2018. Magenta rectangles denote the areas used for the projection of Figure 11.

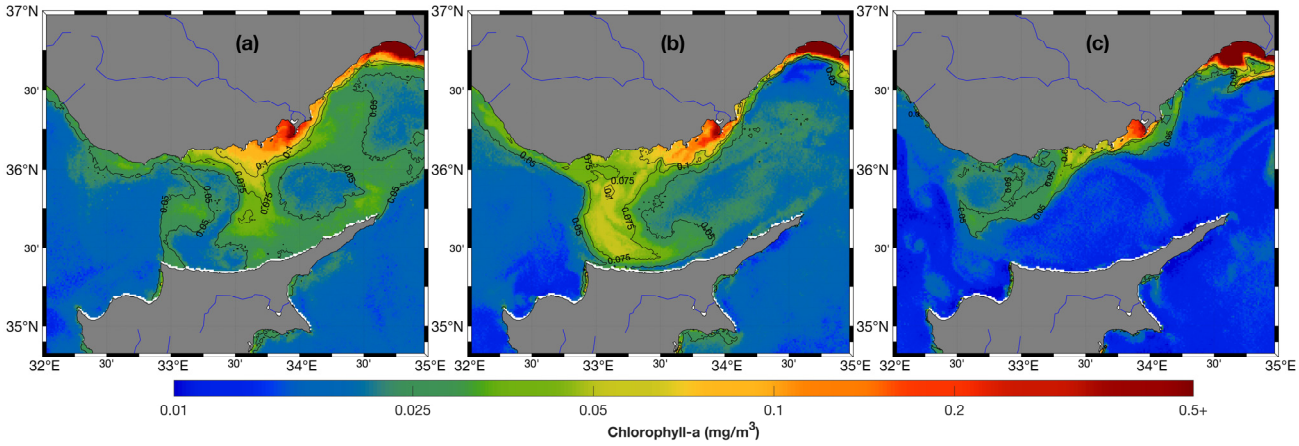



**Figure 11.** Chlorophyll-a distribution in the Cilician Basin for (**a**) 2 June 2018, (**b**) 14 July 2018, and (**c**) 13 August 2018. Map projections represent the areas denoted by the magenta rectangles in Figure 10d–f.

Cross-shelf transport via eddies was observed throughout the summer of 2018, whereas in 2020 they were limited. In 2018, kinetic energy was low in July and August (Figure 12)

in comparison to the climatology values (Figure S2). Conversely, in July and August of 2020, the kinetic energy was higher than the climatology. The high kinetic energy in 2020 indicates the strengthening of the AMC and corresponds to higher SST gradient magnitudes (Figure 13). In 2020, strong frontal gradients were observed along the coastline (Figure 13). As a result of the high kinetic energy and increased frontal gradients in 2020, cross-shelf transport was inhibited.

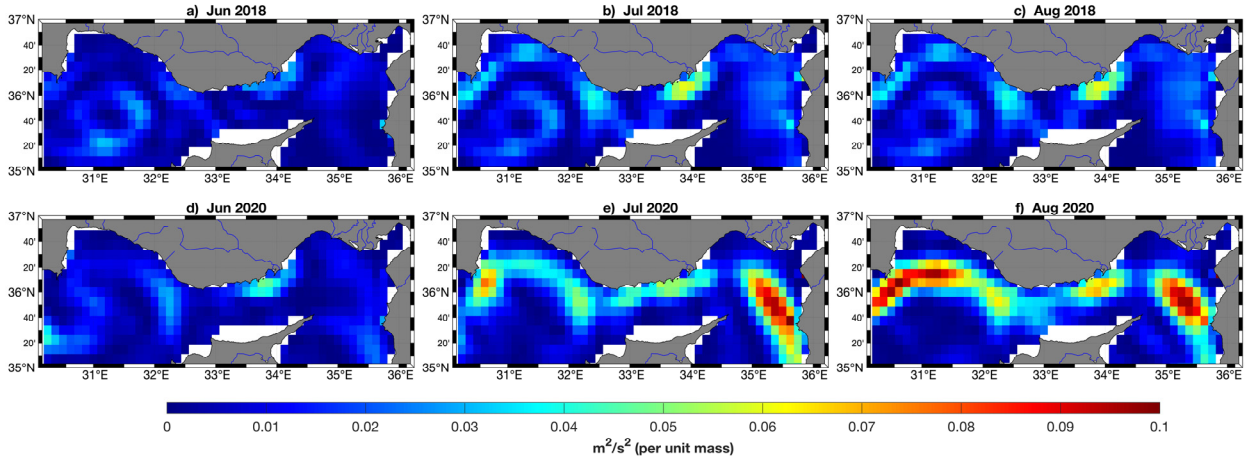



**Figure 12.** Kinetic energy (per unit mass) in the northeastern Levantine waters for (**a**) June 2018, (**b**) July 2018, (**c**) August 2018, (**d**) June 2020, (**e**) July 2020, and (**f**) August 2020.

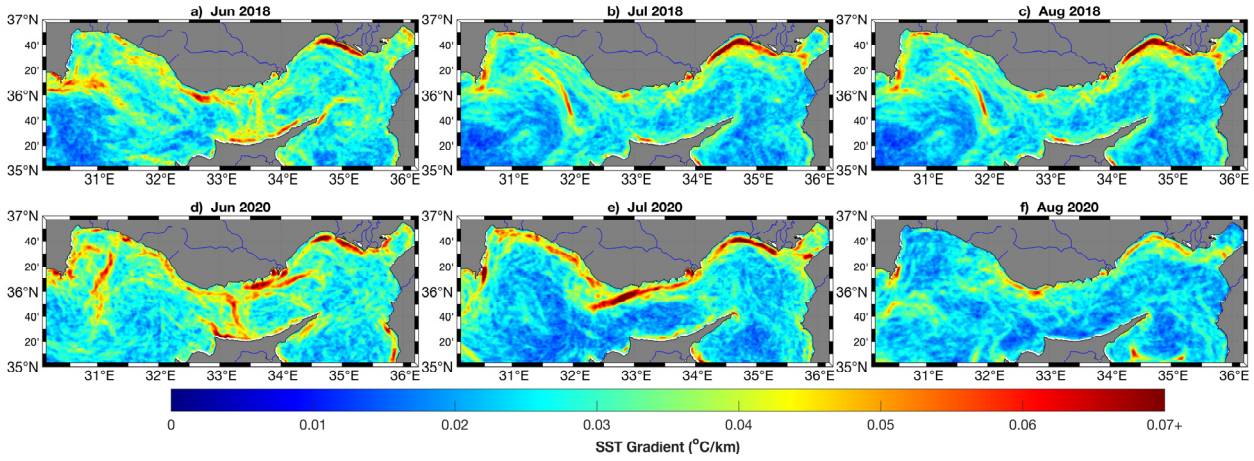



**Figure 13.** SST gradients in the northeastern Levantine waters for (**a**) June 2018, (**b**) July 2018, (**c**) August 2018, (**d**) June 2020, (**e**) July 2020, and (**f**) August 2020.

## 4. Discussion

The present study focuses on the Levantine Basin of the Mediterranean Sea, which has gone through changes including increases in sea level, salinity, temperature, and freshwater fluxes [14], increasing the interannual variability of the circulation. Hence, the variability of the circulation over the course of 20 years (2003–2022) is likely the reason for the standard deviations (Figure 4) observed in the seasonal climatology of the SST gradients. Standard deviations of similar magnitudes were also documented in a different region over a similarly long time series [35].

Higher seasonal SST gradient magnitudes are observed (Figure 4) around well-known circulation features [33,45], particularly around the cyclonic conduit [14]. This is expected, as frontal patterns often represent circulation patterns [52].

In winter, strong SST gradients are found in the north, due to extensive winter convection in this region [53]. Spring has the lowest SST gradients, coincident with reduced

wind forcing and heat loss, as well as a low-sea level anomaly [48]. Summer intensification of SST gradients likely occurs due to the difference in warming rates of coastal/riverine waters vs. deep waters, as well as increased Ekman pumping due to upwelling favorable winds. The patterns of high summer SST gradients shown here (Figure 4) correspond to summer upwelling areas [54].

FP is calculated using the Canny algorithm, which depends on two thresholds to define the fronts. The thresholds are determined using the distribution of the dataset (PDF, Figure 2). Regardless of how they are determined, the choice of thresholds may alter the resulting frontal probability (FP). However, the FP spatial distributions presented here (Figure 5) are in agreement with those of a previous study that used a histogram-based approach [29]. The FP spatial distributions (Figure 5) are also coherent with the SST gradient distributions on a seasonal scale, and they show that fronts are likely to occur all over the basin (FP > 0). FP is presented here only at seasonal intervals; thus, areas with low seasonal frontal probability can have higher FPs calculated over higher frequencies (e.g., monthly). Monthly FPs are not presented in this study, as they are inherently noisy due to the impact of sub-mesoscale features, which typically have a temporal scale of 1–5 days [55].

EOF-1 (Figure 6) represents SST gradient features in the western part of the Levantine Basin, around Ierapetra and Rhodes. PC1 (Figure 6d) follows PC1-WSC (Figure 7d) with 3–4 months of lag, indicating the delayed response of the SST gradients to intensified WSC. This lag likely corresponds to the intensification of circulation following strong winds, as documented for Ierapetra eddies in particular, which intensify within 4 months following the onset of strong winds [49].

The increased WSC (PC1-WSC, Figure 7d) during the 2005–2008 period corresponds to the maxima of the SST gradients, with the strongest gradients observed around the Rhodes Gyre and Ierapetra eddies. Previous studies confirm the presence of strong Ierapetra eddies in this period [49], with lifetimes exceeding one year after their formation [50]. The strongest SST gradients were observed in 2006, which had the maximum WSC in summer and reduced heat loss in winter. Similar to 2006, 2013 had a strong WSC magnitude, but its SST gradients were lower. The main difference between these two years was the heat loss in winter; in the winter of 2013, much more heat was lost to the atmosphere compared to 2006. Hence, we speculate that a weak winter (i.e., reduced heat loss) followed by strong summer winds results in intense annual gradients.

The maximum winter heat loss was observed in 2017; consequently, the lowest SST gradients were observed in spring. The maxima of 2006 and minima of 2017 were also observed in the basin-averaged annual mean SST gradients, indicating the basin-wide influence of the WSC and HF patterns. The variability in wind and heat flux explains only some of the observed variability in seasonal SST gradients, as other factors (e.g., river discharges, topography) also have an influence on the SST gradients.

The interannual EOFs (Figure 9) represent a reduction in SST gradients (EOF1-INT) and an increase in gradients mostly in the northern Levantine waters (EOF2-INT) for 2003–2022. EOF1-INT shows the significance of the general cyclonic circulation and well-known circulation features beyond seasonal scales. Overall, EOF1-INT (Figure 9) explains most of the variability, showing a reduction in SST gradients that corresponds to the basin-wide reduction in cyclonic circulation after 2015 [18]. This is also confirmed by the basin-averaged annual means of the SST gradients (Figure 8).

PC2-INT (Figure 9c) shows an increase after 2017, which represents a strengthening of the coastal fronts, particularly in the northern Levantine waters (Figure 9b), thereby inhibiting cross-shelf exchange. However, EOF2-INT explains only 17.6% of the total variance and only represents the SST gradient variability at the surface, but cross-shelf exchange also occurs below the surface. Hence, further analysis is necessary to confirm whether EOF2-INT corresponds to a strengthening of coastal fronts and a consequent reduction in cross-shelf exchange.

The Asia Minor Current, known for its thermal gradients, was investigated in the Cilician Basin, where increased anticyclonic activity is typically observed in summer [45].

However, in the summer of 2020, the presence of eddies was reduced and the AMC was more pronounced, as confirmed by higher kinetic energy (Figure 12) and stronger SST gradients (Figure 13). Meanwhile, the weaker AMC in 2018 corresponded to an increased presence of eddies, including anticyclones and cyclone/anticyclone dipoles, resulting in eddy-induced cross-shelf transport, as indicated by the chlorophyll-a images (Figure 11). Hence, SST gradients are an indicator of boundary current strength. An intensified boundary current (i.e., front) inhibits cross-shelf transport. Here, only a section of the AMC is shown as an example, but similar eddy-mediated cross-shelf transport can be observed in the remotely sensed sea surface height, temperature, and chlorophyll-a images, particularly along the coastlines of Israel, Lebanon, Syria, and Türkiye. This cross-shelf transport is important for the oligotrophic waters of the Mediterranean, and its reduction could influence the ecosystem. Therefore, future efforts would ideally focus on quantifying cross-shelf transport in the Levantine Basin, similar to studies conducted in other shelf seas [56–59].

## 5. Conclusions

In this study, SST fronts were investigated, presenting their seasonal climatology as well as their temporal and spatial variability. Overall, high frontal activity was observed in the northern Levantine waters, especially around well-known circulation features such as the Rhodes Gyre and Ierapetra eddies, and around ROFI.

This spatial distribution of seasonal frontal activity was confirmed by frontal probability, which shows the likelihood of frontal occurrence in the same areas.

EOF analysis revealed the seasonal variability in the SST gradients, as well as the WSC and HF. The seasonal variability in SST gradients is correlated with wind and heat flux. PC1 of the SST gradients is correlated with PC1-WSC (r = 0.72, with 4 months of lag), and PC2 of the SST gradients is correlated with PC1-HF (r =0.84).

Typically, the strongest SST gradients are observed after warm winters followed by intense summer winds. Intense winter cooling reduces SST gradients. The greatest frontal activity was observed in 2006, and the least in 2017. The SST gradients decreased after 2015 in most of the Levantine Basin, consistent with the reduction in cyclonic circulation. The secondary mode of the interannual EOF analysis indicated a slight increase in SST gradients, particularly in the northern Levantine waters, but this explains only a small amount of the total variance.

Increased frontal gradients indicate a stronger boundary current. The Asia Minor Current (AMC) is presented as an example boundary current. The summers of 2018 and 2020 are presented as examples, which had different kinetic energy and frontal gradients. It was found that years with low kinetic energy (e.g., 2018) are accompanied by reduced frontal gradients, resulting in cross-shelf transport, whereas years with high kinetic energy (e.g., 2020) are accompanied by increased frontal gradients, inhibiting cross-shelf transport. Frontal instabilities of the boundary current (i.e., the Asia Minor Current) and associated cross-shelf transports are currently under investigation and will be presented subsequently.

**Supplementary Materials:** The following supporting information can be downloaded at: https://www.mdpi.com/article/10.3390/jmse12081249/s1, Figure S1: Example sequence of frontal detection methodology for a daily SST image (a) SST. (b) SST Gradients. (c) Fronts detected using Canny algorithm; Figure S2: Monthly climatology of Kinetic Energy (per unit mass) in the northern Levantine; Figure S3: Monthly climatology of SST gradients in the northern Levantine; Figure S4: Monthly climatology of SST in the northern Levantine.

**Funding:** This publication is part of the project "Impacts of Climate Change on Ocean Frontal Ecosystems (ClimaFront)," funded by the Turkish Scientific and Technological Research Council (TÜBİTAK) and the European Commission Horizon 2020 Marie Skłodowska-Curie Actions Co-fund program "Co-Funded Brain Circulation2 Scheme (CoCirculation2)." This publication has been produced benefiting from the 2236 Co-Funded Brain Circulation Scheme2 (CoCirculation2) of TÜBİTAK (Project No: 121C411). However, the entire responsibility for this publication/paper belongs to the owner of the publication/paper. The financial support received from TÜBİTAK does not mean that the

content of this publication was approved in a scientific sense by TÜBİTAK. The author also acknowledges support from "DEKOSIM" (BAP-08-11-DPT2012K120880), funded by the Turkish Ministry of Development, and the "Integrated Marine Pollution Monitoring Program of the Mediterranean" project (2020-09-00-2-00-009), supported by the Turkish Ministry of Environment, Urbanization and Climate Change.

**Institutional Review Board Statement:** Not Applicable.

**Informed Consent Statement:** Not Applicable.

**Data Availability Statement:** MUR-SST data are available at https://podaac.jpl.nasa.gov/dataset/MUR-JPL-L4-GLOB-v4.1 (accessed on 1 March 2024). Heat flux and wind data are available from the Copernicus Climate Change Service (DOI: 10.24381/cds.f17050d7). Neither the European Commission nor the ECMWF is responsible for any use that may be made of the Copernicus information or the data it contains. Absolute dynamic topography and geostrophic velocity data are available at https://doi.org/10.48670/moi-00141 (accessed on 28 March 2024). Satellite chlorophyll-a data are available from https://doi.org/10.48670/moi-00300 (accessed on 1 April 2024). All datasets used in this study were last accessed on 1 June 2024.

**Acknowledgments:** I would like to thank Bettina Fach for their constructive criticism and discussion.

**Conflicts of Interest:** The author declares no conflicts of interest. The funders had no role in the design of the study; in the collection, analyses, or interpretation of data; in the writing of the manuscript; or in the decision to publish the results.

## References

1. Belkin, I.M.; Cornillon, P.C.; Sherman, K. Fronts in Large Marine Ecosystems. *Prog. Oceanogr.* **2009**, *81*, 223–236. [CrossRef]
2. Belkin, I.M. Remote Sensing of Ocean Fronts in Marine Ecology and Fisheries. *Remote Sens.* **2021**, *13*, 883. [CrossRef]
3. Mahadevan, A. Modeling Vertical Motion at Ocean Fronts: Are Nonhydrostatic Effects Relevant at Submesoscales? *Ocean Model.* **2006**, *14*, 222–240. [CrossRef]
4. Chelton, D.B.; Xie, P.; Chelton, D.B.; Xie, S.P. Coupled Ocean-Atmosphere Interaction at Oceanic Mesoscales. *Oceanogr. Mag.* **2010**, *23*, 52–69. [CrossRef]
5. Wang, Y.; Castelao, R.M.; Yuan, Y. Seasonal Variability of Alongshore Winds and Sea Surface Temperature Fronts in E Astern B Oundary C Urrent S Ystems. *J. Geophys. Res. Ocean.* **2015**, *120*, 2385–2400. [CrossRef]
6. Wang, Y.; Castelao, R.M. Variability in the Coupling between Sea Surface Temperature and Wind Stress in the Global Coastal Ocean. *Cont. Shelf Res.* **2016**, *125*, 88–96. [CrossRef]
7. Ibrahim, O.; Mohamed, B.; Nagy, H. Spatial Variability and Trends of Marine Heat Waves in the Eastern Mediterranean Sea over 39 Years. *J. Mar. Sci. Eng.* **2021**, *9*, 643. [CrossRef]
8. Hamdeno, M.; Alvera-Azcaráte, A. Marine Heatwaves Characteristics in the Mediterranean Sea: Case Study the 2019 Heatwave Events. *Front. Mar. Sci.* **2023**, *10*, 1093760. [CrossRef]
9. Simon, A.; Plecha, S.M.; Russo, A.; Teles-Machado, A.; Donat, M.G.; Auger, P.-A.; Trigo, R.M. Hot and Cold Marine Extreme Events in the Mediterranean over the Period 1982–2021. *Front. Mar. Sci.* **2022**, *9*, 892201. [CrossRef]
10. Juza, M.; Fernández-Mora, À.; Tintoré, J. Sub-Regional Marine Heat Waves in the Mediterranean Sea From Observations: Long-Term Surface Changes, Sub-Surface and Coastal Responses. *Front. Mar. Sci.* **2022**, *9*, 785771. [CrossRef]
11. Aboelkhair, H.; Mohamed, B.; Morsy, M.; Nagy, H. Co-Occurrence of Atmospheric and Oceanic Heatwaves in the Eastern Mediterranean over the Last Four Decades. *Remote Sens.* **2023**, *15*, 1841. [CrossRef]
12. Deliceırmak, Ç.; Salihoğlu, İ. Physical Oceanographic Features of the Cilician Basin and Wastewater Dumping at the Coastal Zone of Kyrenia. *Desalin. Water Treat.* **2020**, *177*, 290–296. [CrossRef]
13. Pisano, A.; Marullo, S.; Artale, V.; Falcini, F.; Yang, C.; Leonelli, F.E.; Santoleri, R.; Buongiorno Nardelli, B. New Evidence of Mediterranean Climate Change and Variability from Sea Surface Temperature Observations. *Remote Sens.* **2020**, *12*, 132. [CrossRef]
14. Menna, M.; Gačić, M.; Martellucci, R.; Notarstefano, G.; Fedele, G.; Mauri, E.; Gerin, R.; Poulain, P.-M. Climatic, Decadal, and Interannual Variability in the Upper Layer of the Mediterranean Sea Using Remotely Sensed and In-Situ Data. *Remote Sens.* **2022**, *14*, 1322. [CrossRef]
15. Menna, M.; Gerin, R.; Notarstefano, G.; Mauri, E.; Bussani, A.; Pacciaroni, M.; Poulain, P.-M. On the Circulation and Thermohaline Properties of the Eastern Mediterranean Sea. *Front. Mar. Sci.* **2021**, *8*, 671469. [CrossRef]
16. Fach, B.A.; Orek, H.; Yilmaz, E.; Tezcan, D.; Salihoglu, I.; Salihoglu, B.; Latif, M.A. Water Mass Variability and Levantine Intermediate Water Formation in the Eastern Mediterranean between 2015 and 2017. *J. Geophys. Res. Ocean.* **2021**, *126*, e2020JC016472. [CrossRef]
17. Zodiatis, G.; Brenner, S.; Gertman, I.; Ozer, T.; Simoncelli, S.; Ioannou, M.; Savva, S. Twenty Years of In-Situ Monitoring in the South-Eastern Mediterranean Levantine Basin: Basic Elements of the Thermohaline Structure and of the Mesoscale Circulation during 1995-2015. *Front. Mar. Sci.* **2023**, *9*, 1074504. [CrossRef]

18. Grodsky, S.A.; Reul, N.; Bentamy, A.; Vandemark, D.; Guimbard, S. Eastern Mediterranean Salinification Observed in Satellite Salinity from SMAP Mission. *J. Mar. Syst.* **2019**, *198*, 103190. [CrossRef]
19. Kubin, E.; Poulain, P.-M.; Mauri, E.; Menna, M.; Notarstefano, G. Levantine Intermediate and Levantine Deep Water Formation: An Argo Float Study from 2001 to 2017. *Water* **2019**, *11*, 1781. [CrossRef]
20. Ozer, T.; Rahav, E.; Gertman, I.; Sisma-Ventura, G.; Silverman, J.; Herut, B. Relationship between Thermohaline and Biochemical Patterns in the Levantine Upper and Intermediate Water Masses, Southeastern Mediterranean Sea (2013–2021). *Front. Mar. Sci.* **2022**, *9*, 958924. [CrossRef]
21. Ozer, T.; Gertman, I.; Gildor, H.; Herut, B. Thermohaline Temporal Variability of the SE Mediterranean Coastal Waters (Israel)—Long-Term Trends, Seasonality, and Connectivity. *Front. Mar. Sci.* **2022**, *8*, 799457. [CrossRef]
22. Meroni, A.N.; Giurato, M.; Ragone, F.; Pasquero, C. Observational Evidence of the Preferential Occurrence of Wind Convergence over Sea Surface Temperature Fronts in the Mediterranean. *Q. J. R. Meteorol. Soc.* **2020**, *146*, 1443–1458. [CrossRef]
23. Desbiolles, F.; Alberti, M.; Hamouda, M.E.; Meroni, A.N.; Pasquero, C. Links Between Sea Surface Temperature Structures, Clouds and Rainfall: Study Case of the Mediterranean Sea. *Geophys. Res. Lett.* **2021**, *48*, e2020GL091839. [CrossRef]
24. Sudre, F.; Hernández-Carrasco, I.; Mazoyer, C.; Sudre, J.; Dewitte, B.; Garçon, V.; Rossi, V. An Ocean Front Dataset for the Mediterranean Sea and Southwest Indian Ocean. *Sci. Data* **2023**, *10*, 730. [CrossRef] [PubMed]
25. Barral, Q.-B.; Zakardjian, B.; Dumas, F.; Garreau, P.; Testor, P.; Beuvier, J. Characterization of Fronts in the Western Mediterranean with a Special Focus on the North Balearic Front. *Prog. Oceanogr.* **2021**, *197*, 102636. [CrossRef]
26. Nencioli, F.; Petrenko, A.A.; Doglioli, A.M. Diagnosing Cross-shelf Transport along an Ocean Front: An Observational Case Study in the Gulf of Lion. *J. Geophys. Res. Ocean.* **2016**, *121*, 7218–7243. [CrossRef]
27. Royer, F.; Fromentin, J.; Gaspar, P. Association between Bluefin Tuna Schools and Oceanic Features in the Western Mediterranean. *Mar. Ecol. Prog. Ser.* **2004**, *269*, 249–263. [CrossRef]
28. Yalçin, E. The Behaviour of Turkish Bluefin Tuna (Thunnus Thynnus) Fishing Fleet in the Mediterranean Sea. *Mar. Sci. Technol. Bull.* **2019**, *8*, 64–68. [CrossRef]
29. Mauzole, Y.L. Objective Delineation of Persistent SST Fronts Based on Global Satellite Observations. *Remote Sens. Environ.* **2022**, *269*, 112798. [CrossRef]
30. Akpınar, A.; Fach, B.A. Sea Surface Temperature Fronts in the Levantine Basin of the Mediterranean Sea. In Proceedings of the EGU General Assembly 2023, Vienna, Austria, 24–28 April 2023; p. EGU23-3361. [CrossRef]
31. Chin, T.M.; Vazquez-Cuervo, J.; Armstrong, E.M. A Multi-Scale High-Resolution Analysis of Global Sea Surface Temperature. *Remote Sens. Environ.* **2017**, *200*, 154–169. [CrossRef]
32. Robinson, A.R.; Malanotte-Rizzoli, P.; Hecht, A.; Michelato, A.; Roether, W.; Theocharis, A.; Ünlüata, Ü.; Pinardi, N.; Artegiani, A.; Bergamasco, A.; et al. General Circulation of the Eastern Mediterranean. *Earth-Sci. Rev.* **1992**, *32*, 285–309. [CrossRef]
33. Poulain, P.-M.; Menna, M.; Mauri, E. Surface Geostrophic Circulation of the Mediterranean Sea Derived from Drifter and Satellite Altimeter Data. *J. Phys. Oceanogr.* **2012**, *42*, 973–990. [CrossRef]
34. Canny, J. A Computational Approach to Edge Detection. *IEEE Trans. Pattern Anal. Mach. Intell.* **1986**, *6*, 679–698. [CrossRef]
35. Saldías, G.S.; Hernández, W.; Lara, C.; Muñoz, R.; Rojas, C.; Vásquez, S.; Pérez-Santos, I.; Soto-Mardones, L. Seasonal Variability of SST Fronts in the Inner Sea of Chiloé and Its Adjacent Coastal Ocean, Northern Patagonia. *Remote Sens.* **2021**, *13*, 181. [CrossRef]
36. Volpe, G.; Buongiorno Nardelli, B.; Colella, S.; Pisano, A.; Santoleri, R. An Operational Interpolated Ocean Colour Product in the Mediterranean Sea. In *New Frontiers in Operational Oceanography*; Chassignet, E.P., Pascual, A., Tintoré, J., Verron, J., Eds.; CreateSpace Independent Publishing Platform: Scotts Valley, CA, USA, 2018; ISBN 978-1-72054-997-0.
37. Volpe, G.; Colella, S.; Brando, V.E.; Forneris, V.; La Padula, F.; Di Cicco, A.; Sammartino, M.; Bracaglia, M.; Artuso, F.; Santoleri, R. Mediterranean Ocean Colour Level 3 Operational Multi-Sensor Processing. *Ocean Sci.* **2019**, *15*, 127–146. [CrossRef]
38. Berthon, J.-F.; Zibordi, G. Bio-Optical Relationships for the Northern Adriatic Sea. *Int. J. Remote Sens.* **2004**, *25*, 1527–1532. [CrossRef]
39. Hersbach, H.; Bell, B.; Berrisford, P.; Hirahara, S.; Horányi, A.; Muñoz-Sabater, J.; Nicolas, J.; Peubey, C.; Radu, R.; Schepers, D.; et al. The ERA5 Global Reanalysis. *Q. J. R. Meteorol. Soc.* **2020**, *146*, 1999–2049. [CrossRef]
40. Copernicus Climate Change Service, Copernicus Climate Change Service (C3S) Climate Data Store (CDS). ERA5 Hourly Data on Single Levels from 1940 to Present. Available online: https://cds.climate.copernicus.eu/cdsapp#!/dataset/10.24381/cds.adbb2d47?tab=overview (accessed on 7 March 2023).
41. GEBCO Compilation Group. GEBCO 2023 Grid. Available online: https://www.gebco.net/data_and_products/gridded_bathymetry_data/gebco_2023/ (accessed on 1 March 2024).
42. Pawlowicz, R. M_Map: A Mapping Package for "MATLAB", Version 1.4m. Available online: https://www.eoas.ubc.ca/~rich/map.html (accessed on 1 March 2024).
43. Thyng, K.; Greene, C.; Hetland, R.; Zimmerle, H.; DiMarco, S. True Colors of Oceanography: Guidelines for Effective and Accurate Colormap Selection. *Oceanography* **2016**, *29*, 9–13. [CrossRef]
44. Greene, C.A.; Thirumalai, K.; Kearney, K.A.; Delgado, J.M.; Schwanghart, W.; Wolfenbarger, N.S.; Thyng, K.M.; Gwyther, D.E.; Gardner, A.S.; Blankenship, D.D. The Climate Data Toolbox for MATLAB. *Geochem. Geophys. Geosyst.* **2019**, *20*, 3774–3781. [CrossRef]
45. Özsoy, E.; Hecht, A.; Ünlüata, Ü.; Brenner, S.; Oğuz, T.; Bishop, J.; Latif, M.A.; Rozentraub, Z. A Review of the Levantine Basin Circulation and Its Variability during 1985–1988. *Mediterr. Sea* **1991**, *15*, 421–456. [CrossRef]

46. Marullo, S.; Santoleri, R.; Malanotte-Rizzoli, P.; Bergamasco, A. The Sea Surface Temperature Field in the Eastern Mediterranean from Advanced Very High Resolution Radiometer (AVHRR) Data: Part I. Seasonal Variability. *J. Mar. Syst.* **1999**, *20*, 63–81. [CrossRef]
47. Marullo, S.; Nardelli, B.B.; Guarracino, M.; Santoleri, R. Observing the Mediterranean Sea from Space: 21 Years of Pathfinder-AVHRR Sea Surface Temperatures (1985 to 2005): Re-Analysis and Validation. *Ocean Sci.* **2007**, *3*, 299–310. [CrossRef]
48. Amitai, Y.; Lehahn, Y.; Lazar, A.; Heifetz, E. Surface Circulation of the Eastern Mediterranean Levantine Basin: Insights from Analyzing 14 Years of Satellite Altimetry Data. *J. Geophys. Res. Ocean.* **2010**, *115*, 2010JC006147. [CrossRef]
49. Ioannou, A.; Stegner, A.; Le Vu, B.; Taupier-Letage, I.; Speich, S. Dynamical Evolution of Intense Ierapetra Eddies on a 22 Year Long Period. *J. Geophys. Res. Ocean.* **2017**, *122*, 9276–9298. [CrossRef]
50. Ioannou, A.; Stegner, A.; Dubos, T.; Le Vu, B.; Speich, S. Generation and Intensification of Mesoscale Anticyclones by Orographic Wind Jets: The Case of Ierapetra Eddies Forced by the Etesians. *J. Geophys. Res. Ocean.* **2020**, *125*, e2019JC015810. [CrossRef]
51. Ioannou, A.; Stegner, A.; Dumas, F.; Le Vu, B. Three-Dimensional Evolution of Mesoscale Anticyclones in the Lee of Crete. *Front. Mar. Sci.* **2020**, *7*, 609156. [CrossRef]
52. Belkin, I.M.; Cornillon, P.C. *Fronts in the World Ocean's Large Marine Ecosystems*; ICES CM 2007/D:21; International Council for the Exploration of the Sea: Copenhagen, Denmark, 2007.
53. Josey, S.A.; Schroeder, K. Declining Winter Heat Loss Threatens Continuing Ocean Convection at a Mediterranean Dense Water Formation Site. *Environ. Res. Lett.* **2023**, *18*, 024005. [CrossRef]
54. Bakun, A.; Agostini, V.N. Seasonal Patterns of Wind-Induced Upwelling/Downwelling in the Mediterranean Sea. *Sci. Mar.* **2001**, *65*, 243–257. [CrossRef]
55. Solodoch, A.; Barkan, R.; Verma, V.; Gildor, H.; Toledo, Y.; Khain, P.; Levi, Y. Basin-Scale to Submesoscale Variability of the East Mediterranean Sea Upper Circulation. *J. Phys. Oceanogr.* **2023**, *53*, 2137–2158. [CrossRef]
56. Zhou, F.; Shapiro, G.; Wobus, F. Cross-Shelf Exchange in the Northwestern Black Sea. *J. Geophys. Res. Ocean.* **2014**, *119*, 2143–2164. [CrossRef]
57. Akpınar, A.; Sadighrad, E.; Fach, B.A.; Arkın, S. Eddy Induced Cross-Shelf Exchanges in the Black Sea. *Remote Sens.* **2022**, *14*, 4881. [CrossRef]
58. Li, J.; Qiao, L.; Zhong, Y.; Xue, W.; Yang, H. Cross-Shelf Transport off the Northern Taiwan, East China Sea. *Estuar. Coast. Shelf Sci.* **2023**, *293*, 108513. [CrossRef]
59. Mou, L.; Niu, Q.; Xia, M. The Roles of Wind and Baroclinic Processes in Cross-Isobath Water Exchange within the Bohai Sea. *Estuar. Coast. Shelf Sci.* **2022**, *274*, 107944. [CrossRef]


**Disclaimer/Publisher's Note:** The statements, opinions and data contained in all publications are solely those of the individual author(s) and contributor(s) and not of MDPI and/or the editor(s). MDPI and/or the editor(s) disclaim responsibility for any injury to people or property resulting from any ideas, methods, instructions or products referred to in the content.